3 Microstructural Characterization

The microstructures of Ni–alloy weld metals such as Alloys 182 and 82 are similar in composition to those of wrought Alloys 600 and 690. Under certain thermal treatments, Cr–rich carbides can precipitate at both interdendrite and intradendrite grain boundaries.[31] Chromium depletion also occurs at the boundaries that are covered with such carbides. The precipitate phases are predominantly $M_{23}C_6$ and Ti–rich MC carbide. During the welding process, only the $M_{23}C_6$ carbide precipitates because of the rapid cooling of the weld metal from fusion temperature. Nucleation of M_7C_3 carbides requires long periods at relatively high temperatures, whereas nucleation of $M_{23}C_6$ is quite rapid and cannot be avoided even during water quenching from solution treatment temperatures. The matrix also contains a uniform dispersion of spherical γ' phase (Ni_3Ti).

The greater susceptibility of Alloy 182 to SCC than Alloy 82 has been attributed to differences in Cr depletion observed in the two alloys because of differences in their composition. Alloy 182 contains higher concentrations of C and Fe and a lower concentration of Cr, all of which enhance Cr depletion during carbide precipitation.

The current section presents the metallography of the weld alloys used in the CGR tests. The SEM and EDX investigations focused on the double-J weld, while the OIM analysis was conducted on both double-J and deep-groove laboratory prepared welds.

3.1 Weld Microstructure

A metallographic examination was performed to characterize the microstructure of the weld. For this purpose, three 1 cm × 2 cm rectangular pieces, designated 1, 2, and 3, were cut from the weld, as shown in Fig. 7. The thickness of all three samples was 0.5 cm. Sample 3 was further cut in half to enable the examination of both surfaces A and B, normal to the plane of Fig. 7.

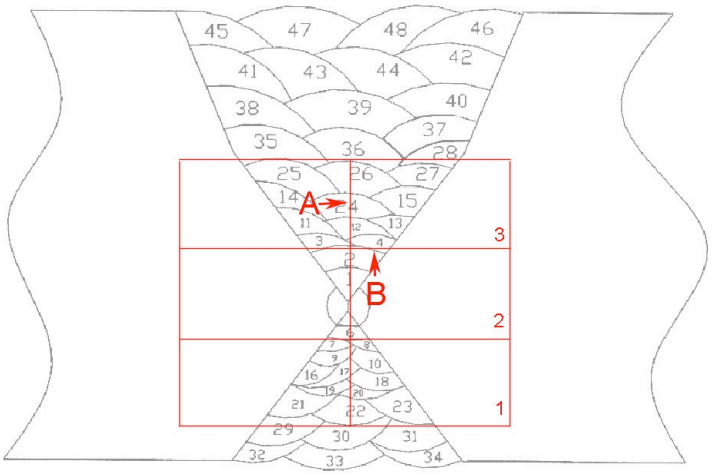

Figure 7. Schematic showing the locations of the three samples cut from the weld.

All samples were mechanically polished through 1–μm diamond paste, followed by electrolytic etching for 10–20 s in a 70% H_3PO_4 and water solution at 5 V to reveal the dendritic structure and carbides. The samples were then examined in a JEOL scanning electron microscope. Figure 8a shows the entire span of the weld microstructure on Sample 1 (the picture shown here was rotated by 90°

counter clockwise with respect to the schematic shown in Fig. 7 to fit in the page). The elongated grains with dendritic features are easily discernible from the regular microstructure of Alloy 600 (upper-left and bottom-left corners). This difference is also visible in Fig. 8b. Figures 8c and 8d also show the dendritic microstructure in the weld. Large variations in grain size can be observed between the different passes.

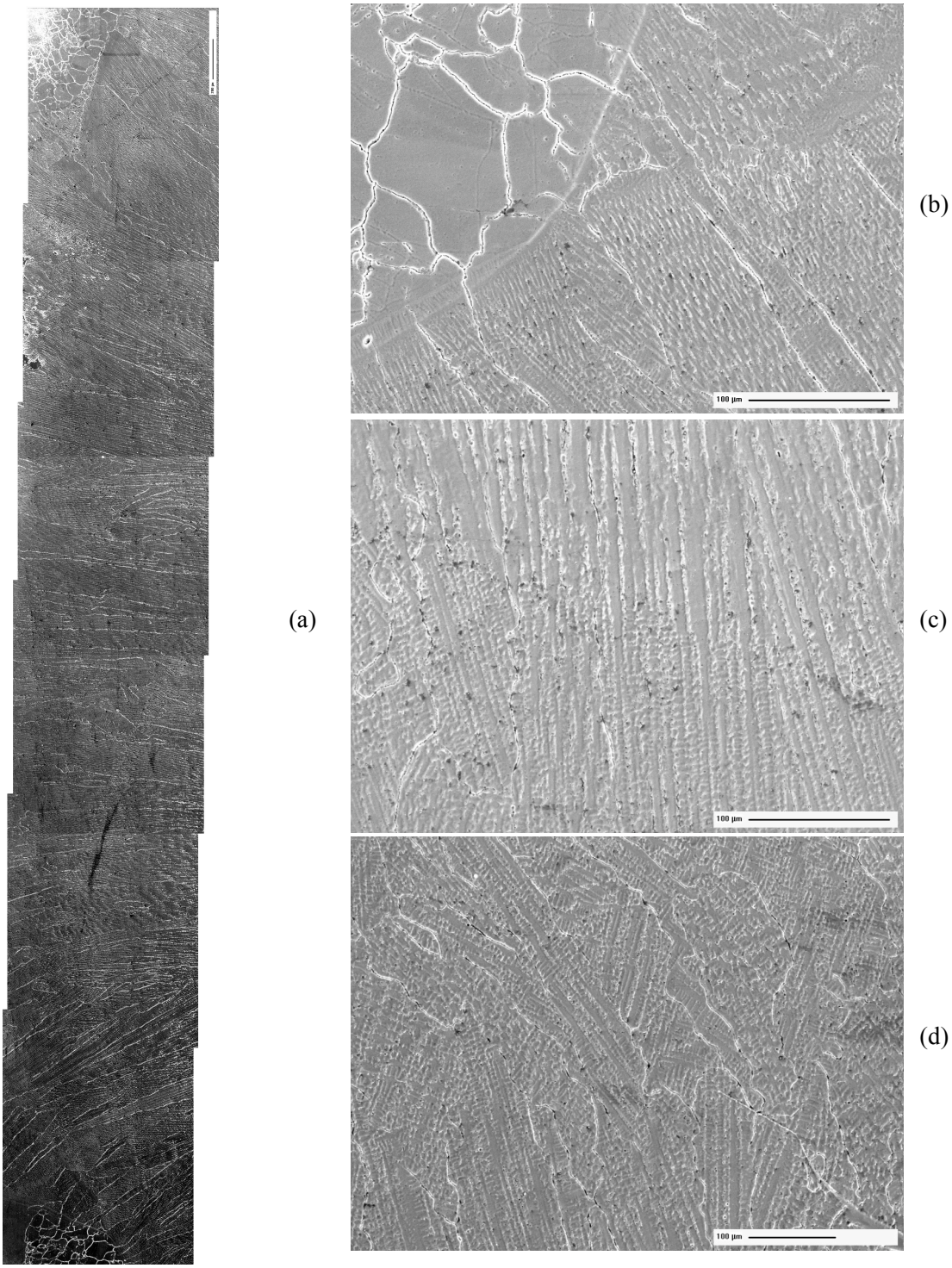

Figure 8. (a) Weld microstructure from Sample 1 (rotated 90° with respect to Fig. 7); (b) transition area between the weld and Alloy 600; and (c, d) dendritic microstructure in the weld.

Figure 9 focuses on the transition area between the weld and the base material, i.e., the heat affected zone (HAZ). A larger grain size than that of the base material is observed in the immediate vicinity of the well in both Figs. 9a and 9b. These micrographs were obtained from opposite locations on Sample 1. A dendritic microstructure was observed on the plane 3A (Fig. 7), and examples are shown in Fig. 10. The picture shown in Fig. 10a was taken at a location where the grain is still visible, although with internal dendritic features. Figure 10b was obtained at a weld pass, showing the different structure of the two weld layers.

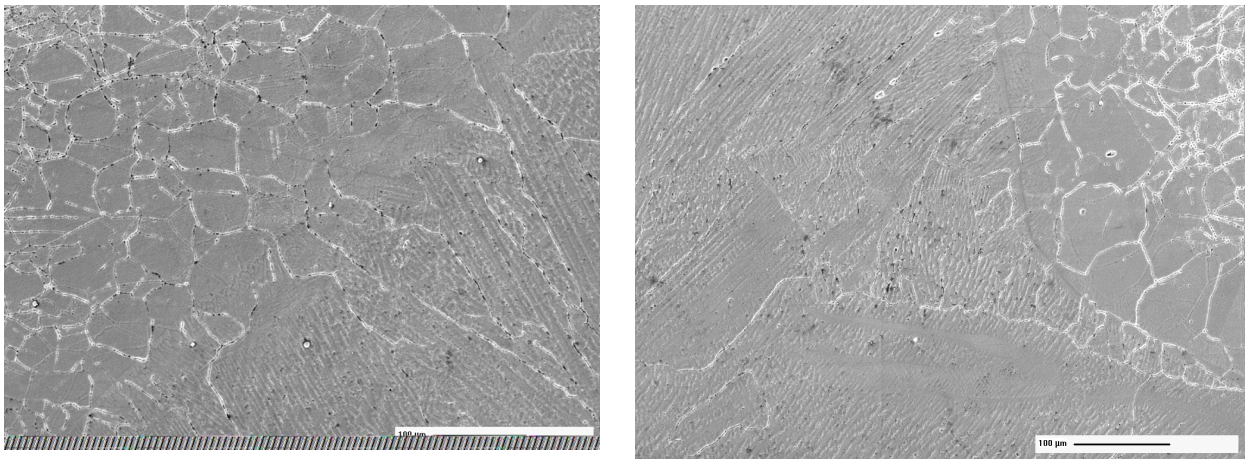

(a) (b)

Figure 9. Large grain microstructure in the HAZ at two opposite positions (a and b).

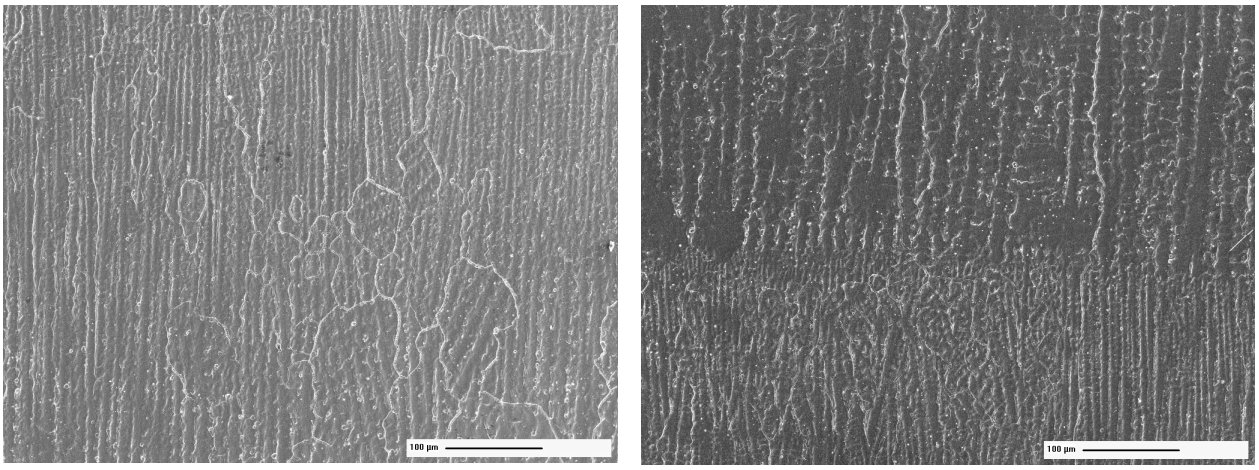

(a) (b)

Figure 10. Dendritic microstructure (a) on sample 3A and (b) at a weld pass.

Figure 11a and 11b are micrographs obtained on plane 3B at weld passes. Figure 11c and 11d are higher magnification micrographs obtained at locations shown in Figs. 11a and 11b, respectively. The grain and dendritic microstructures are visible; however, as expected, the grains are more regular and the dendrites are perpendicular to the plane of observation.

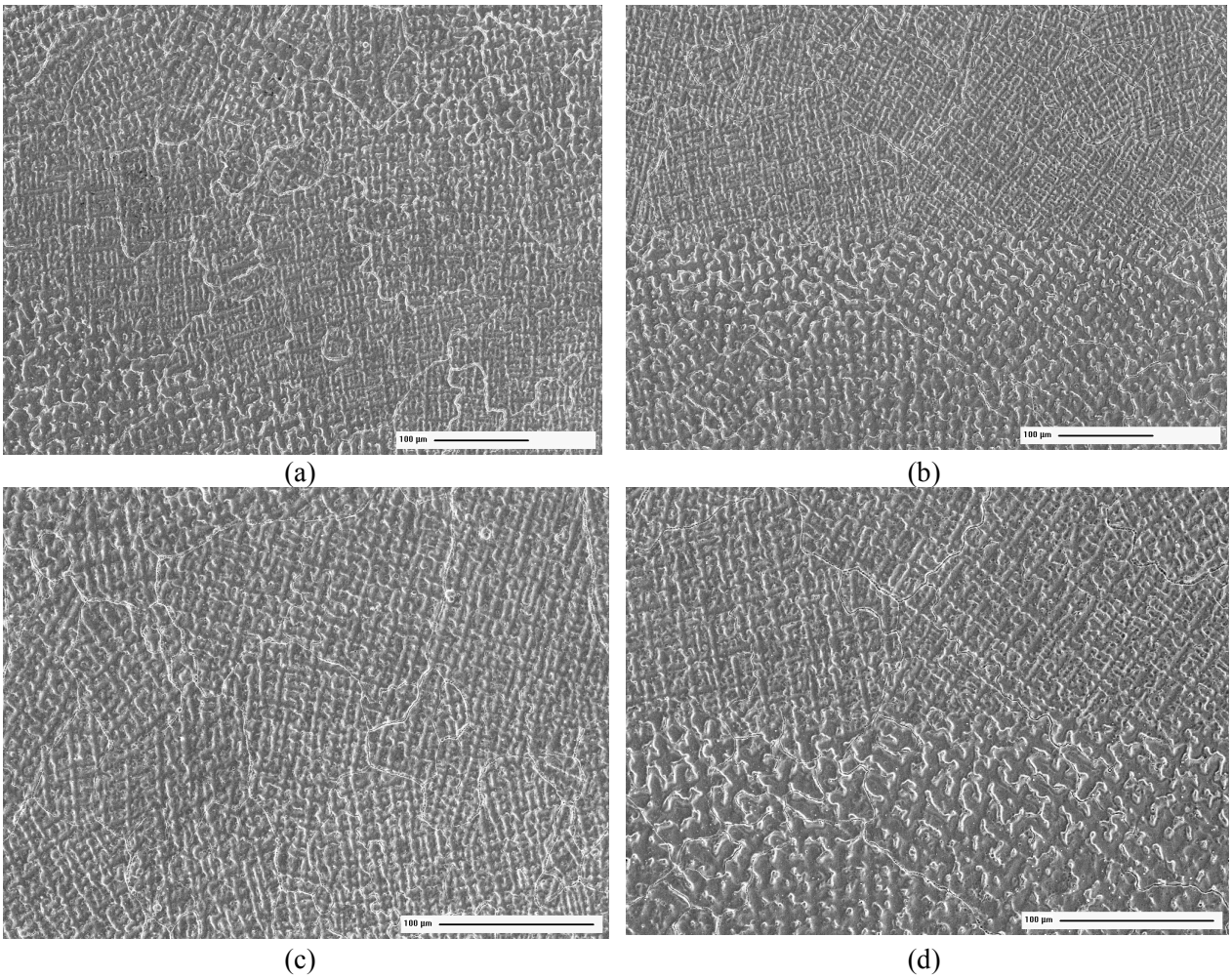

(a) (b)

(c) (d)

Figure 11. Dendritic microstructure at weld passes on sample 3B (a, b) and high magnification micrographs at the respective locations (c, d).

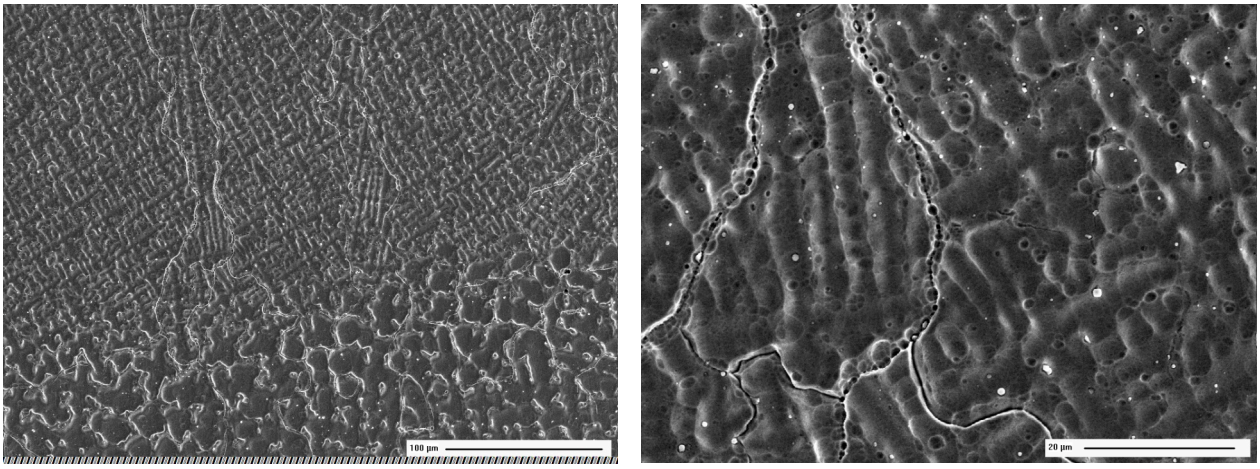

(a) (b)

Figure 12. (a) Dendritic microstructure on sample 3B and (b) high magnification of a region from (a).

Figure 12a is another example of the microstructure obtained on plane 3B at a weld pass, and Fig. 12b is a higher magnification micrograph obtained at a location in Fig. 12a. From the manner in which the phosphoric acid attacked the grain boundaries it appears that grain boundary precipitates were present. Additional precipitates or particles were also observed in grain boundaries and matrix, which had not been attacked by the phosphoric–acid etch.

3.2 Examination of Weld by SEM/EDX

Scanning electron microscopy and energy dispersive x–ray (SEM/EDX) analysis was conducted on sample 3A in a Philips XL30 FEG SEM. This sample was mechanically polished to 1–µm diamond paste, followed by electrolytic etching in a phosphoric–acid solution to reveal the dendritic structure and carbides. Figures 13a–b show the microstructure observed on the surface of sample 3A, at several magnifications. The elongated grains with dendritic features can be seen in both micrographs.

The objective of this part of the analysis was to investigate the nature of both matrix and grain boundary precipitates. Figure 14a shows one of the matrix precipitates on the surface of sample 3A. In Fig. 14b the EDX spectra resulting from the bulk and the precipitate are shown. The comparison of the two spectra indicates that both the Ti and O peaks are higher in the spectrum resulting from the precipitate, suggesting that the particle composition is TiO_2. The results of the analysis are shown in Table 3, confirming that indeed the precipitates are TiO_2.

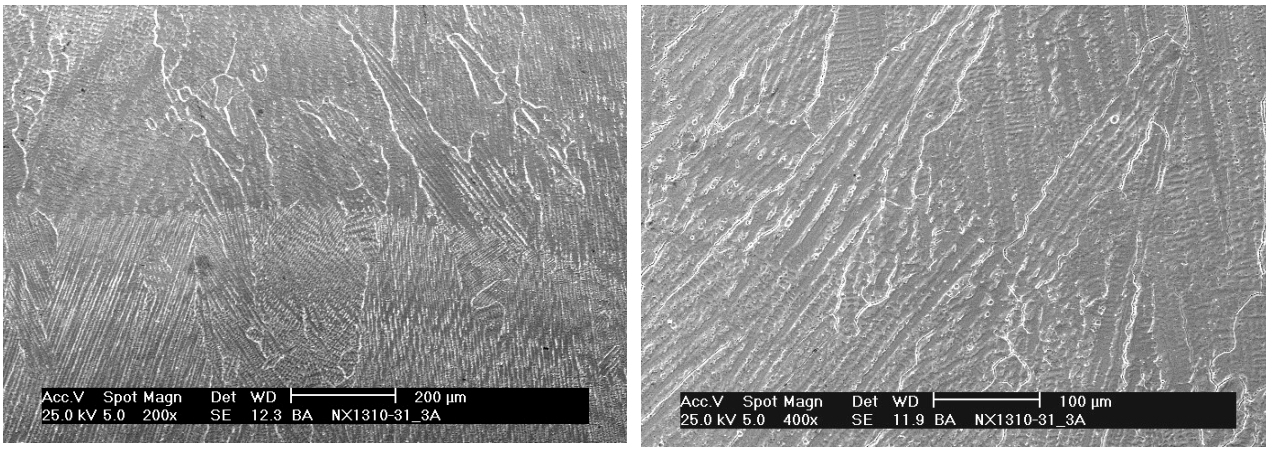

(a) (b)

Figure 13. Dendritic microstructure observed on the surface of sample 3A at magnifications of (a) 100×, (b) 200×.

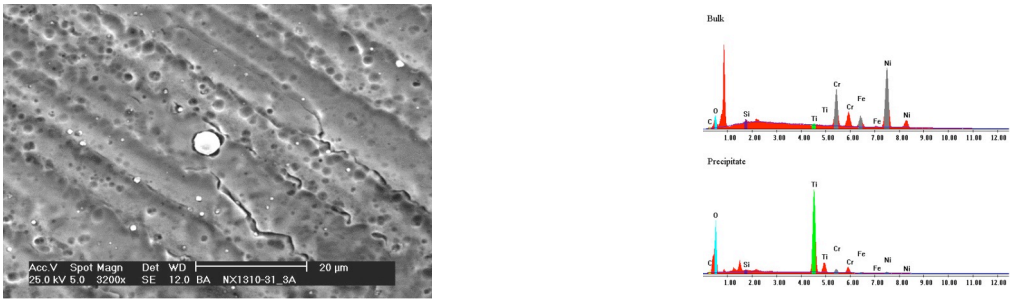

(a) (b)

Figure 14. (a) Micrograph showing one of the matrix precipitates observed on the surface of sample 3A and (b) EDX spectra resulting from the bulk and the precipitate shown in (a).

Table 3. Chemical compositions of the bulk and matrix precipitate resulting from EDX analysis.

Element	Bulk		Matrix precipitate	
	wt. %	at. %	wt. %	at. %
C	1.53	6.56	1.66	3.63
O	**1.77**	**5.72**	**39.08**	**64.24**
Si	0.60	1.10	0.56	0.52
Ti	**0.48**	**0.52**	**50.15**	**27.54**
Cr	15.20	15.08	3.83	1.94
Fe	7.30	6.74	1.06	0.50
Ni	73.12	64.27	3.67	1.64
Total	100.00	100.00	100.00	100.00

Next, the nature of the grain boundary precipitates was investigated. Figure 15a shows the microstructure on plane "A" (Fig. 7), while Fig. 15b is a higher magnification micrograph showing both matrix and grain boundary precipitates. In Fig. 15c EDX spectra resulting from the bulk and from one the grain boundary precipitate are shown. Again, the comparison of the two spectra and the quantitative results shown in Table 4 suggest that the grain boundary precipitate is TiO_2.

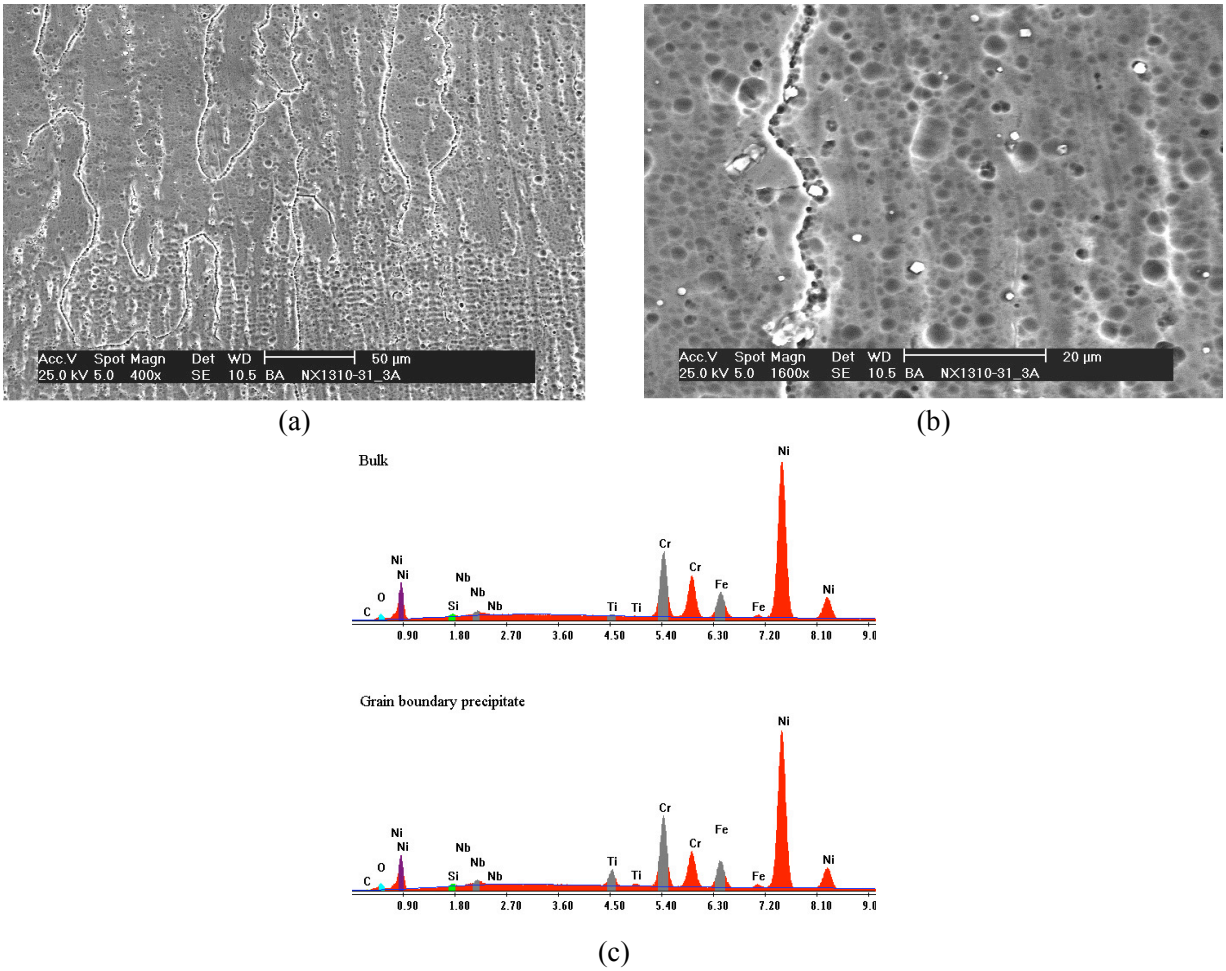

Figure 15. Micrographs showing (a) the microstructure on plane 3A, (b) matrix and grain boundary precipitates, and (c) EDX spectra resulting from the bulk and grain boundary precipitates.

Table 4. Chemical compositions of the bulk and grain boundary precipitate resulting from EDX analysis.

	Bulk		GB precipitate	
Element	wt. %	at. %	wt. %	at. %
C	1.34	5.82	1.65	6.99
O	**1.94**	**6.33**	**2.25**	**7.18**
Si	0.75	1.39	0.62	1.13
Nb	2.14	1.20	2.26	1.24
Ti	**0.30**	**0.32**	**2.70**	**2.87**
Cr	14.23	14.26	14.73	14.44
Fe	7.27	6.78	7.41	6.76
Ni	72.03	63.90	68.38	59.38
Total	100.00	100.00	100.00	100.00

The microstructure on plane "A" (Fig. 7) was further examined in a Hitachi S-4700 field emission gun SEM, allowing a close inspection of the precipitates and grain boundary continuity across the HAZ. Figures 16a, c are high magnification micrographs showing Ti-rich precipitates in the weld material, in both matrix and grain boundaries. Figures 16b, d, are maps showing the topography at the locations where the high magnification micrographs were taken. One observes that both grain boundary and matrix precipitates appear to stick out from the sample surface, thus were not attached by the etch.

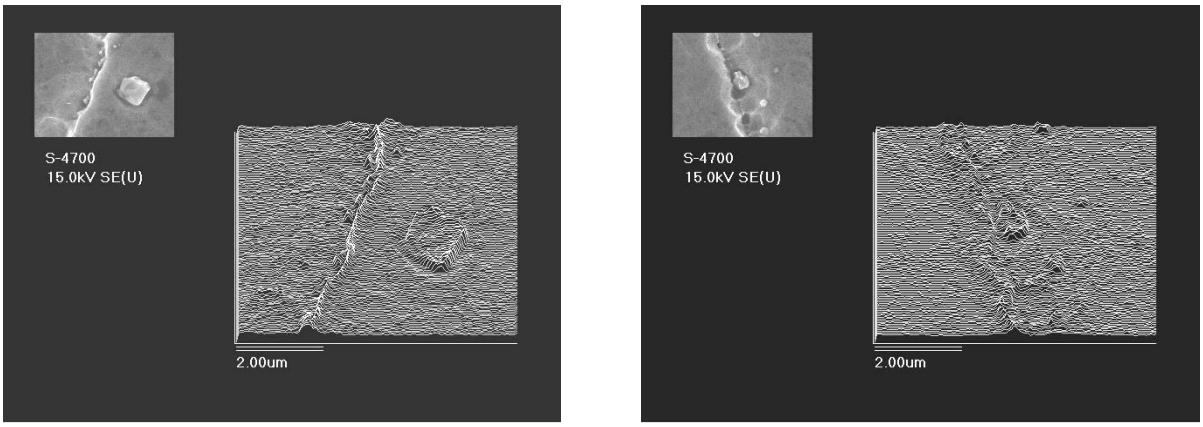

(a) (b)

Figure 16. Examples of Ti-rich precipitates in the weld (top left) and maps showing the topography at the locations where the high magnification micrographs were taken.

Figures 17a and c show areas on the HAZ where the dendritic microstructure (lower left) is replaced by the large grains of the HAZ. Figures 17b and d are high magnification micrographs of the precipitates observed in Figs. 17a and c, respectively. Figure 17 also shows that, as suggested by the depth of the etch attack, random boundaries from the weld extend into the HAZ.

In summary, the metallographic examination of the weld alloy has found that there exists a large variation in grain size between the different weld passes. Both matrix and grain boundary precipitates were observed, and these were identified to be TiO_2. The effect of TiO_2 precipitates on the SCC behavior is unknown. High angle boundaries were observed to extend from the weld into the HAZ, and the implication of this observation is that once a crack initiates in the HAZ, it can then readily extend into the weld via such continuous, cracking-susceptible boundaries.

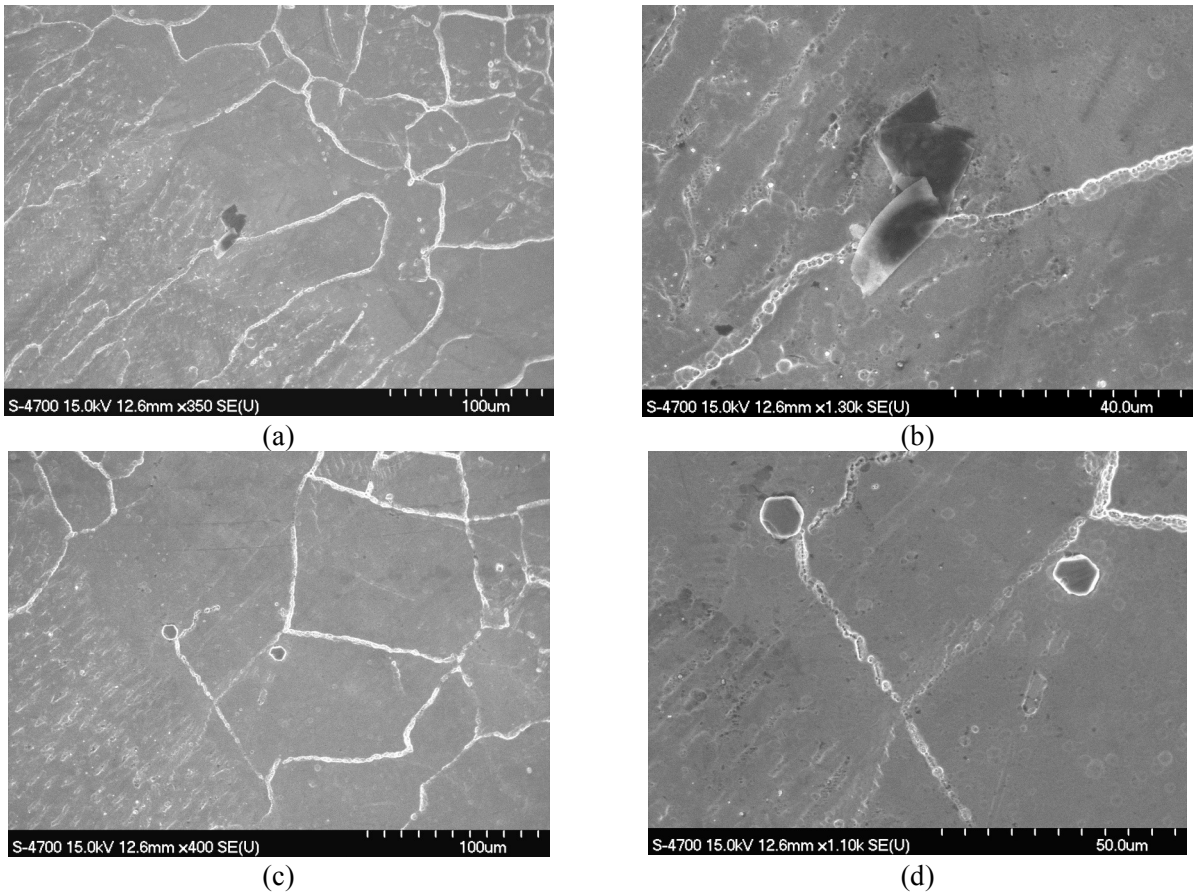

Figure 17. Micrographs showing the heat–affected zone (a, c) and high magnification micrographs showing precipitates in the heat–affected zone (b, d).

3.3 Examination of Weld Specimens by Orientation Imaging Microscopy

Orientation imaging microscopy (OIM) is a diffraction-based technique by which maps of the crystal structure of a material can be obtained, thus determining both the orientations of the grains and the types of grain boundaries present. Intergranular SCC behavior of austenitic alloys in high–temperature aqueous environments is known to be strongly influenced by the proportions of boundaries in special orientation relationships and the magnitude and location of residual stress.[32–35] Thus the information provided by the OIM analysis can give insights into the relative susceptibility of specific welds or components.

First, specimens from the double-J weld were examined by OIM. A specimen was cut and polished to reveal both the surface plane and plane "B" (see Fig. 7). The sample was polished with 1–μm diamond paste and electro-polished in a perchloric acid (10%) and methanol solution at –50°C. Repeated double polishing cycles of 5 s at 40 V provided the best surface finish.

Figure 18a shows an OIM map resulting from the weld, plane B. In this analysis, the grain boundaries were classified as either low angle boundaries (LAB, $\Sigma = 1$), coincident site lattice boundaries (CSLB, $3 \leq \Sigma < 29$), or high angle boundaries (HAB, $\Sigma \geq 29$), where Σ represents the reciprocal of the density of coincident sites. For example, a $\Sigma 3$ boundary designates a boundary where 1 in every 3 sites on one grain coincides with a site from the adjacent grain. In terms of angle/axis misorientation, to achieve this particular coincidence, one grain must be rotated by 60° around the [111] direction. For the

current work Brandon's criterion[36] was used to determine the maximum allowed deviation from exact coincidence: $\delta\theta=15^\circ\ \Sigma^{1/2}$. According to Brandon's criterion the maximum allowed misorientation for a Σ1 boundary is 15°, and for a Σ3 is 8.6°.

Cracking would be expected along the high angle boundaries, identified as such in the OIM map, Fig. 18a. Also displayed (Fig. 18b) is a map showing the crystal directions parallel (±15°) to the normal to the sample surface. We first noticed that the dendritic structure does not appear in the OIM maps, suggesting that the dendrites are coherent and, therefore, very unlikely to crack. Overall, the appearance is that plane B exhibits little or no texture (Fig. 18b). Figure 18c consists of two tables. The upper table shows the legend for the grain directions as well as the resulting fractions of grains having a certain direction. The lower table shows the legend for CSL boundaries, resulting boundary fractions of each type, and the misorientation distribution function (MDF) values, and are a distribution of misorientations measured at grain boundaries and area-weighted.

We observed that the fraction of cracking-resistant CSLBs is very low, 26%. For comparison, solution–annealed Alloy 600 has a CSLB fraction of approximately 50%. If this last observation holds true for a larger area – where a statistically significant number of boundaries are analyzed – it would suggest a high degree of susceptibility of the weld.

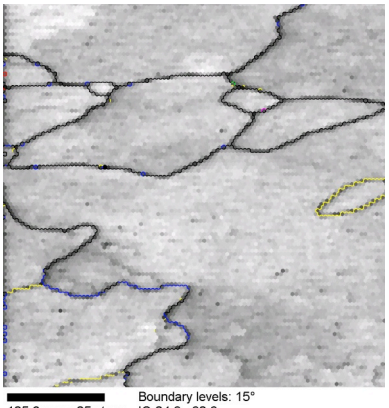

(a)

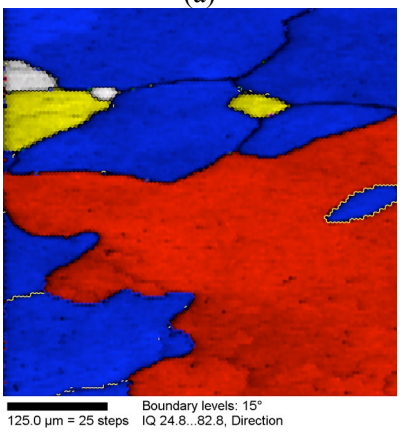

(b)

Gray Scale Map Type: Image Quality
24.8...82.8 (24.8...82.8)

Color Coded Map Type: Crystal Direction

Direction	Min	Max	Total Fraction	Partition Fraction
<1 0 0>||[0 0 1]	0°	15°	0.465	0.465
<0 1 1>||[0 0 1]	0°	15°	0.036	0.036
<1 1 1>||[0 0 1]	0°	15°	0.000	0.000
<1 1 2>||[0 0 1]	0°	15°	0.000	0.000
<1 1 4>||[0 0 1]	0°	15°	0.488	0.488

Boundaries: Rotation Angle

Min	Max	Fraction
15°	180°	0.883

Boundaries: CSL

Sigma	Tolerance	Fraction	Volume	MDF Value
1	15.00	0.117	0.0228	5.14
3	8.66	0.005	0.0176	0.26
5	6.71	0.006	0.0123	0.50
7	5.67	0.000	0.0099	0.00
11	4.52	0.005	0.0075	0.72
13a	4.16	0.001	0.0029	0.26
13b	4.16	0.012	0.0039	2.96
15	3.87	0.097	0.0094	10.29
17a	3.64	0.006	0.0020	3.15
17b	3.64	0.006	0.0039	1.58
19a	3.44	0.005	0.0033	1.63
19b	3.44	0.000	0.0022	0.00
21a	3.27	0.000	0.0019	0.00
21b	3.27	0.000	0.0057	0.00
23	3.13	0.000	0.0050	0.00
25a	3.00	0.000	0.0011	0.00
25b	3.00	0.000	0.0044	0.00
9	5.00	0.002	0.0102	0.15
27a	2.89	0.002	0.0020	1.18
27b	2.89	0.000	0.0039	0.00
summary	-	0.264	0.1317	2.01

*For statistics - any point pair with misorientation exceeding 2° is considered a boundary

(c)

Figure 18. (a) OIM map of the weld on plane "B", sample 3B; (b) the same OIM map showing the orientation of each grain; and (c) legends for crystal directions and the resulting grain boundary character distribution.

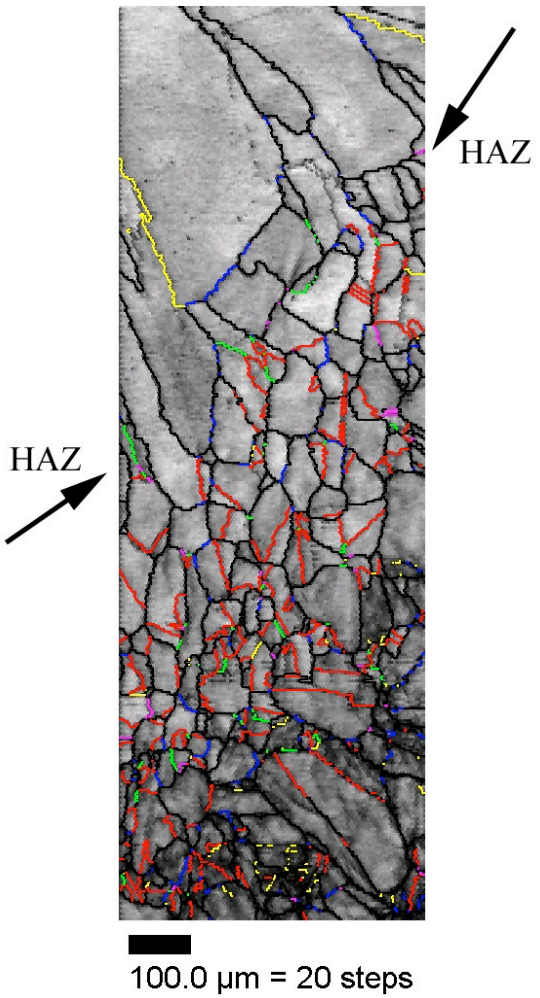

(a)

Gray Scale Map Type: Image Quality
16.9...77.5 (16.9...77.5)

Color Coded Map Type: <none>

Boundaries: Rotation Angle

Min	Max	Fraction
15°	180°	0.966

Boundaries: CSL

Sigma	Tolerance	Fraction	Volume	MDF Value
1	15.00	0.034	0.0228	1.48
3	8.66	0.226	0.0176	12.86
5	6.71	0.006	0.0123	0.45
7	5.67	0.010	0.0099	0.96
11	4.52	0.004	0.0075	0.47
13a	4.16	0.004	0.0029	1.39
13b	4.16	0.007	0.0039	1.70
15	3.87	0.001	0.0094	0.10
17a	3.64	0.001	0.0020	0.74
17b	3.64	0.006	0.0039	1.56
19a	3.44	0.006	0.0033	1.87
19b	3.44	0.001	0.0022	0.31
21a	3.27	0.001	0.0019	0.58
21b	3.27	0.002	0.0057	0.27
23	3.13	0.001	0.0050	0.15
25a	3.00	0.000	0.0011	0.15
25b	3.00	0.002	0.0044	0.52
9	5.00	0.026	0.0102	2.53
27a	2.89	0.005	0.0020	2.52
27b	2.89	0.007	0.0039	1.76
summary	-	0.348	0.1317	2.64

*For statistics - any point pair with misorientation exceeding 10° is considered a boundary

(b)

Figure 19. (a) OIM map on the surface of sample 3B and (b) the resulting grain boundary character distribution. The OIM map covers the weld (upper part), the HAZ (indicated by arrows), and Alloy 600 (lower part).

Next, an area on the surface of the sample was mapped by OIM in the vicinity of the HAZ. The area included the weld, HAZ, and part of the Alloy 600 (Fig. 19a). The resulting proportion of CSLBs was 35%. Although somewhat larger than in the previous example, this proportion appears to be attributable to the inclusion of the area from Alloy 600 in the total count.

Figure 20a shows the same OIM map as Fig. 19a but with the grain directions included. Again, no definitive conclusion can be drawn with respect to the presence or absence of texture in the weld due to the small weld area analyzed. Nevertheless, as in Fig. 18, the OIM did not distinguish the dendritic structure (the SEM micrograph of Fig. 20b was included for comparison). Thus, the grain boundary character distribution will likely determine the cracking behavior of the weld.

The second model weld, the deep-groove weld, was examined by OIM to determine (a) the grain boundary character distribution and (b) any texture in the microstructure. Both these parameters are known to influence the SCC behavior of austenitic alloys in high temperature water environments.[32–40] Specifically, the OIM analysis allows a classification of boundaries according to the coincident site lattice (CSL) model as either CSLB or HAB. The CSLBs are formed when the neighboring grains are in

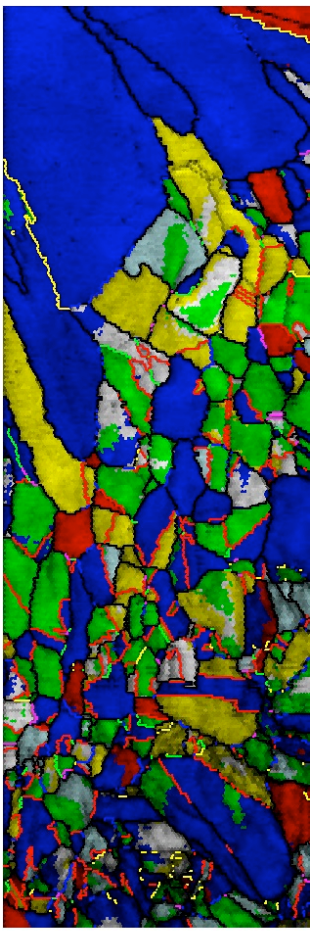

100.0 µm = 20 steps

(a)

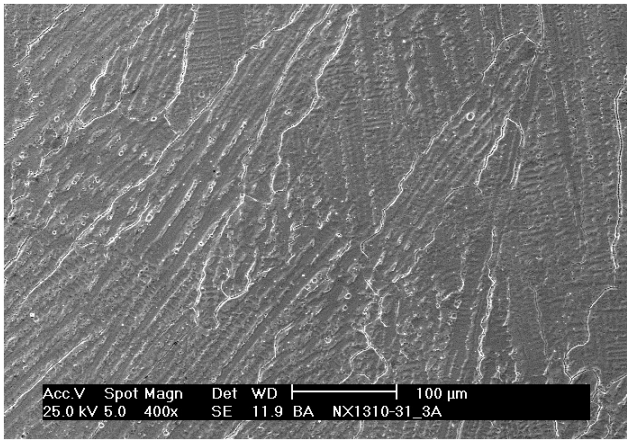

(b)

Color Coded Map Type: Crystal Direction

Direction	Min	Max
<1 0 0>||[0 0 1]	0°	15°
<0 1 1>||[0 0 1]	0°	15°
<1 1 1>||[0 0 1]	0°	15°
<1 1 2>||[0 0 1]	0°	15°
<1 1 4>||[0 0 1]	0°	15°

Figure 20. (a) The same OIM map as in Fig. 19a showing crystal directions and (b) SEM micrograph illustrating the dendritic microstructure of the weld.

specific orientation relationships and have been shown to possess an increased resistance to SCC over HABs.[37] In addition, texture affects the high–temperature deformation behavior of a polycrystalline material and is thus expected to play a role in the SCC behavior as well.

The OIM analysis was carried out on plane "A", along the direction of the dendrites, and "B", perpendicular to the direction of dendrites (Fig. 21). In preparation for the OIM analysis, the weld

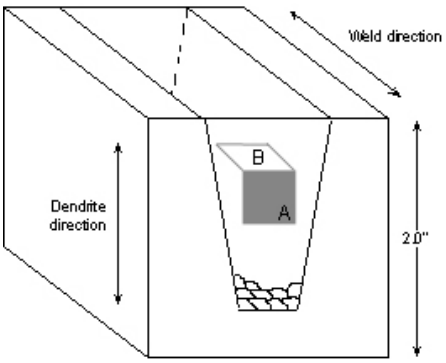

Figure 21.
Schematic showing the two planes on which the OIM characterization was carried out: plane "A", along the direction of the dendrites, and plane "B", perpendicular to the direction of dendrites.

specimens were mechanically polished through 1–µm diamond paste, and electro-polished in a perchloric acid (10%) and methanol solution at –50°C. The OIM characterization was performed in a Philips XL30 FEG SEM equipped with a TexSem OIM system.

Two OIM maps from plane "A" and the corresponding boundary character distributions are shown in Fig. 22. The microstructure (a, c) consists of columnar grains, typical of those observed on this plane. Also, note the absence of dendrites from the OIM map. The boundary character distributions resulting from the two scans (Figs. 22b, d) give CSL fractions of 27.5% and 22.7%.

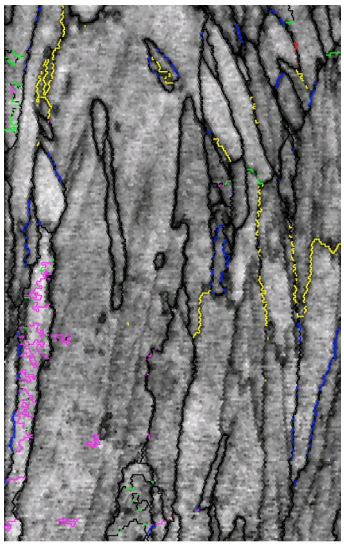

240.0 µm = 30 steps

(a)

Gray Scale Map Type: Image Quality
20.4...50.3 (20.4...50.3)

Color Coded Map Type: <none>

Boundaries: Rotation Angle

Min	Max	Fraction
15°	180°	0.916

Boundaries: CSL

Sigma	Tolerance	Fraction	Volume	MDF Value
1	15.00	0.084	0.0228	3.68
3	8.66	0.002	0.0176	0.09
5	6.71	0.017	0.0123	1.36
7	5.67	0.008	0.0099	0.84
11	4.52	0.000	0.0075	0.07
13a	4.16	0.002	0.0029	0.56
13b	4.16	0.006	0.0039	1.50
15	3.87	0.000	0.0094	0.02
17a	3.64	0.002	0.0020	1.00
17b	3.64	0.004	0.0039	0.92
19a	3.44	0.006	0.0033	1.92
19b	3.44	0.001	0.0022	0.44
21a	3.27	0.014	0.0019	7.38
21b	3.27	0.000	0.0057	0.00
23	3.13	0.001	0.0050	0.13
25a	3.00	0.002	0.0011	1.93
25b	3.00	0.004	0.0044	1.00
9	5.00	0.030	0.0102	3.00
27a	2.89	0.090	0.0020	45.94
27b	2.89	0.002	0.0039	0.46
summary	-	0.275	0.1317	2.09

*For statistics - any point pair with misorientation exceeding 10° is considered a boundary

(b)

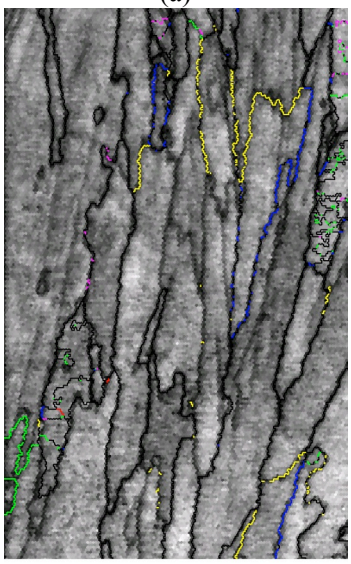

240.0 µm = 30 steps

(c)

Gray Scale Map Type: Image Quality
20.9...51.9 (20.9...51.9)

Color Coded Map Type: <none>

Boundaries: Rotation Angle

Min	Max	Fraction
15°	180°	0.914

Boundaries: CSL

Sigma	Tolerance	Fraction	Volume	MDF Value
1	15.00	0.086	0.0228	3.79
3	8.66	0.002	0.0176	0.11
5	6.71	0.020	0.0123	1.66
7	5.67	0.002	0.0099	0.16
11	4.52	0.000	0.0075	0.02
13a	4.16	0.007	0.0029	2.54
13b	4.16	0.000	0.0039	0.00
15	3.87	0.002	0.0094	0.26
17a	3.64	0.003	0.0020	1.36
17b	3.64	0.000	0.0039	0.00
19a	3.44	0.006	0.0033	1.71
19b	3.44	0.000	0.0022	0.00
21a	3.27	0.033	0.0019	17.41
21b	3.27	0.000	0.0057	0.00
23	3.13	0.000	0.0050	0.00
25a	3.00	0.000	0.0011	0.00
25b	3.00	0.000	0.0044	0.04
9	5.00	0.051	0.0102	5.03
27a	2.89	0.011	0.0020	5.52
27b	2.89	0.004	0.0039	0.90
summary	-	0.227	0.1317	1.73

*For statistics - any point pair with misorientation exceeding 10° is considered a boundary

(d)

Figure 22. OIM maps from plane "A", parallel to the direction of dendrites (a, c), and resulting grain boundary character distributions (b, d).

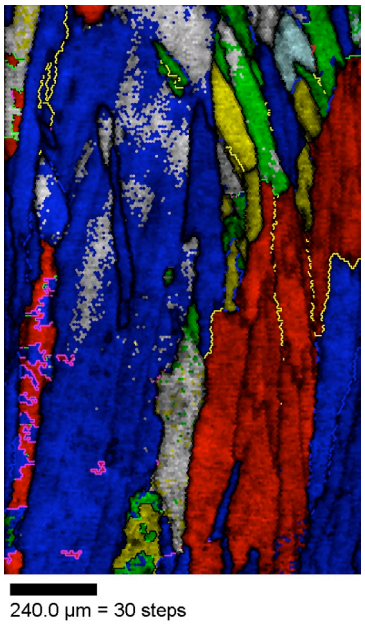

(a)

Gray Scale Map Type: Image Quality
20.4...50.3 (20.4...50.3)

Color Coded Map Type: Crystal Direction

Direction	Min	Max	Total Fraction	Partition Fraction
<1 0 0>||[0 0 1]	0°	15°	0.250	0.250
<0 1 1>||[0 0 1]	0°	15°	0.052	0.052
<1 1 1>||[0 0 1]	0°	15°	0.011	0.011
<1 1 2>||[0 0 1]	0°	15°	0.056	0.056
<1 1 4>||[0 0 1]	0°	15°	0.517	0.517

Boundaries: Rotation Angle

Min	Max	Fraction
15°	180°	0.916

Boundaries: CSL

Sigma	Tolerance	Fraction	Volume	MDF Value
1	15.00	0.084	0.0228	3.68
3	8.66	0.002	0.0176	0.09
5	6.71	0.017	0.0123	1.36
7	5.67	0.008	0.0099	0.84
11	4.52	0.000	0.0075	0.07
13a	4.16	0.002	0.0029	0.56
13b	4.16	0.006	0.0039	1.50
15	3.87	0.000	0.0094	0.02
17a	3.64	0.002	0.0020	1.00
17b	3.64	0.004	0.0039	0.92
19a	3.44	0.006	0.0033	1.92
19b	3.44	0.001	0.0022	0.44
21a	3.27	0.014	0.0019	7.38
21b	3.27	0.000	0.0057	0.00
23	3.13	0.001	0.0050	0.13
25a	3.00	0.002	0.0011	1.93
25b	3.00	0.004	0.0044	1.00
9	5.00	0.030	0.0102	3.00
27a	2.89	0.090	0.0020	45.94
27b	2.89	0.002	0.0039	0.46
summary	-	0.275	0.1317	2.09

*For statistics - any point pair with misorientation exceeding 10° is considered a boundary

(b)

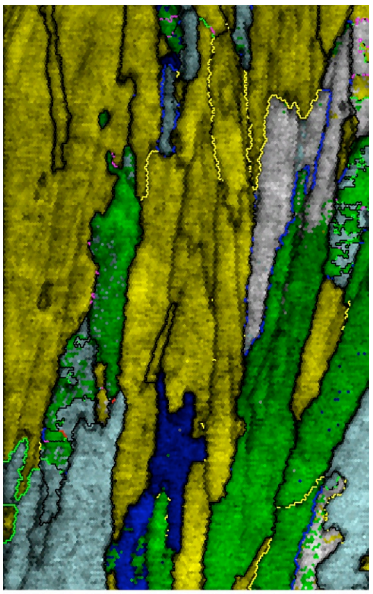

(c)

Gray Scale Map Type: Image Quality
20.9...51.9 (20.9...51.9)

Color Coded Map Type: Crystal Direction

Direction	Min	Max	Total Fraction	Partition Fraction
<1 0 0>||[0 0 1]	0°	15°	0.000	0.000
<0 1 1>||[0 0 1]	0°	15°	0.522	0.522
<1 1 1>||[0 0 1]	0°	15°	0.146	0.146
<1 1 2>||[0 0 1]	0°	15°	0.221	0.221
<1 1 4>||[0 0 1]	0°	15°	0.034	0.034

Boundaries: Rotation Angle

Min	Max	Fraction
15°	180°	0.914

Boundaries: CSL

Sigma	Tolerance	Fraction	Volume	MDF Value
1	15.00	0.086	0.0228	3.79
3	8.66	0.002	0.0176	0.11
5	6.71	0.020	0.0123	1.66
7	5.67	0.002	0.0099	0.16
11	4.52	0.000	0.0075	0.02
13a	4.16	0.007	0.0029	2.54
13b	4.16	0.000	0.0039	0.00
15	3.87	0.002	0.0094	0.26
17a	3.64	0.003	0.0020	1.36
17b	3.64	0.000	0.0039	0.00
19a	3.44	0.006	0.0033	1.71
19b	3.44	0.000	0.0022	0.00
21a	3.27	0.033	0.0019	17.41
21b	3.27	0.000	0.0057	0.00
23	3.13	0.000	0.0050	0.00
25a	3.00	0.000	0.0011	0.00
25b	3.00	0.000	0.0044	0.04
9	5.00	0.051	0.0102	5.03
27a	2.89	0.011	0.0020	5.52
27b	2.89	0.004	0.0039	0.90
summary	-	0.227	0.1317	1.73

*For statistics - any point pair with misorientation exceeding 10° is considered a boundary

(d)

Figure 23. OIM maps from plane “A” (parallel to the direction of dendrites) showing the grain orientations (a, c), and legends for grain orientations and grain boundary character distributions (b, d).

Figure 23a and c present the same OIM maps as Fig. 22, but this time the grain directions are specified. The orientation legend for each map is given next to it (b, d) along with the grain boundary character distributions. For example, a grain shown in red has the [100] direction perpendicular to the plane of the figure, while a grain shown with blue has the [114] direction perpendicular to the plane of the figure. The tolerance angle is 15°. We notice that most of the grains in Fig. 23a have either [100] or [114] directions perpendicular to the sample surface. In addition, the grains sharing similar orientations are also neighbors. A similar observation can be made for the second scan (Fig. 23c). However, in this

map the most prominent directions are [011], and to a lesser extent [111] or [112]. Again, the grains sharing similar orientations appear to be neighbors. Nevertheless, while the material appears not to be textured, note the presence of clusters of grains sharing similar orientations.

Next, plane "B" (perpendicular to the direction of dendrites) was analyzed. Figure 24a shows the resulting OIM map from plane "B", while Fig. 24b also includes the grain orientations. The legend for grain orientation and the corresponding boundary character distributions are shown in Fig. 24c. The microstructure (a) is typical for that observed optically for this plane, and, as previously noted, the dendrites are absent from the OIM map. The resulting CSL fraction for this plane is 29.9% (a, c). Similar to the OIM maps on plane "A", clusters of grains sharing similar orientations can be observed (b).

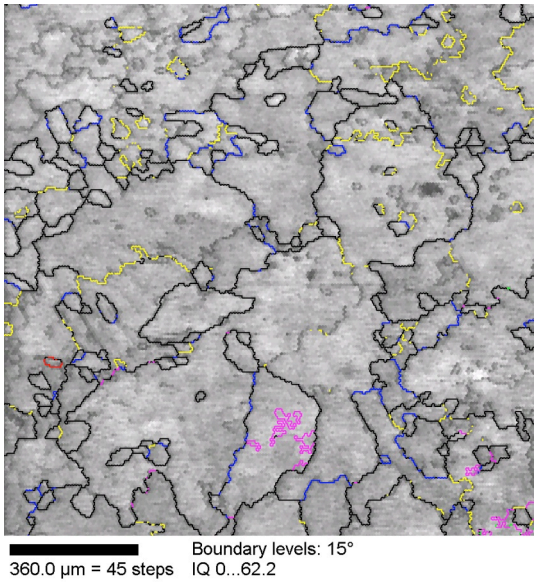

(a)

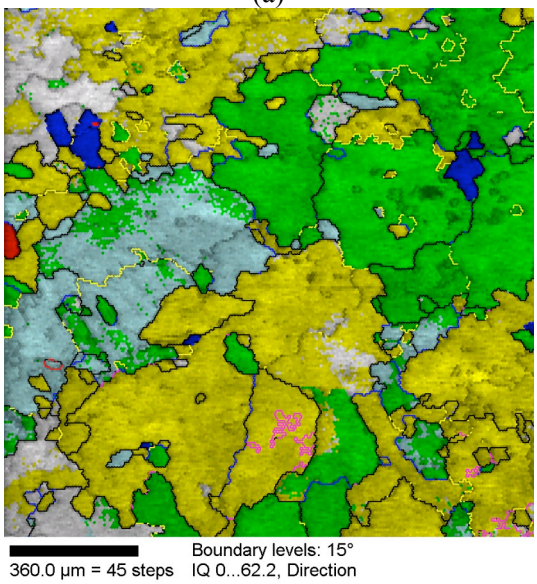

(b)

Gray Scale Map Type: Image Quality
0...62.2 (0...62.2)

Color Coded Map Type: Crystal Direction

Direction	Min	Max	Total Fraction	Partition Fraction
<1 0 0>||[0 0 1]	0°	15°	0.002	0.002
<0 1 1>||[0 0 1]	0°	15°	0.450	0.450
<1 1 1>||[0 0 1]	0°	15°	0.124	0.124
<1 1 2>||[0 0 1]	0°	15°	0.330	0.330
<1 1 4>||[0 0 1]	0°	15°	0.012	0.012

Boundaries: Rotation Angle

Min	Max	Fraction
15°	180°	0.858

Boundaries: CSL

Sigma	Tolerance	Fraction	Volume	MDF Value
1	15.00	0.142	0.0228	6.25
3	8.66	0.003	0.0176	0.15
5	6.71	0.032	0.0123	2.60
7	5.67	0.014	0.0099	1.38
11	4.52	0.003	0.0075	0.39
13a	4.16	0.018	0.0029	6.20
13b	4.16	0.011	0.0039	2.75
15	3.87	0.003	0.0094	0.33
17a	3.64	0.005	0.0020	2.30
17b	3.64	0.001	0.0039	0.14
19a	3.44	0.004	0.0033	1.13
19b	3.44	0.000	0.0022	0.00
21a	3.27	0.001	0.0019	0.34
21b	3.27	0.000	0.0057	0.00
23	3.13	0.009	0.0050	1.90
25a	3.00	0.006	0.0011	5.09
25b	3.00	0.001	0.0044	0.15
9	5.00	0.001	0.0102	0.12
27a	2.89	0.044	0.0020	22.29
27b	2.89	0.004	0.0039	1.10
summary	-	0.299	0.1317	2.27

*For statistics - any point pair with misorientation exceeding 10° is considered a boundary

(c)

Figure 24. OIM map from plane "B", perpendicular to the direction of dendrites (a), map showing the grain orientations (b), and legends for grain orientations and grain boundary character distributions (c).

Figure 25 shows the grain boundary character distribution (GBCD) of the weld alloys. This appears to be dominated by LABs (Σ1). This feature of the weld GBCD is actually consistent with the clustering of grains of similar orientations: one may envision that the higher the proportion of neighboring grains that share some particular orientation, the higher becomes the probability that these grains have parallel crystal structures. The fact that the weld GBCD is dominated by Σ1 boundaries makes it also significantly different from that of Alloy 600, which is dominated by twin-related Σ3, Σ9, and Σ27 boundaries (of which approximately half are coherent).[41]

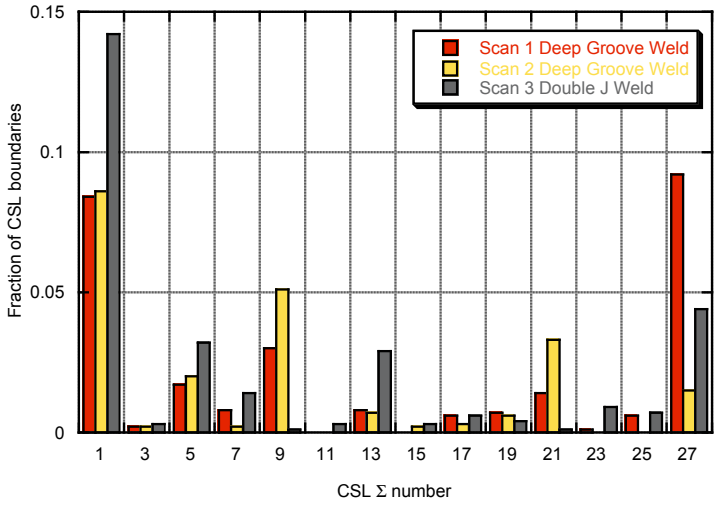

Figure 25.
Grain boundary character distribution for laboratory-prepared welds.

For comparison, the base Alloy 600 was also analyzed by OIM. Figure 26a is an OIM map from this alloy, and Fig. 26b maps the grain orientation. The legend for grain orientation and the corresponding boundary character distributions are shown in Fig. 26c. Unlike the weld alloy, the microstructure shown in Fig 26a is typical of isotropic, solution-annealed Alloy 600. The resulting CSL fraction is 47.1%, close to that generally reported (about 50%) for this alloy in the solution-annealed condition.

In summary, the OIM analysis presented in this section has shown that the intragranular dendrites are coherent and are, therefore, expected to be resistant to cracking. In consequence, it appears that the grain boundary character distribution (along with residual deformation) will determine the cracking behavior of the welds. The proportion of cracking–resistant CSL boundaries in the weld was found to be relatively small; however, the clustering of grains having similar orientations was observed.

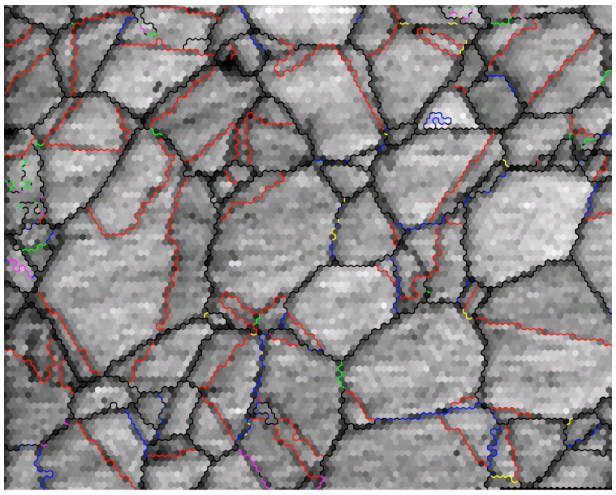

200.0 µm = 25 steps Boundary levels: 15°
IQ 17.2...60

(a)

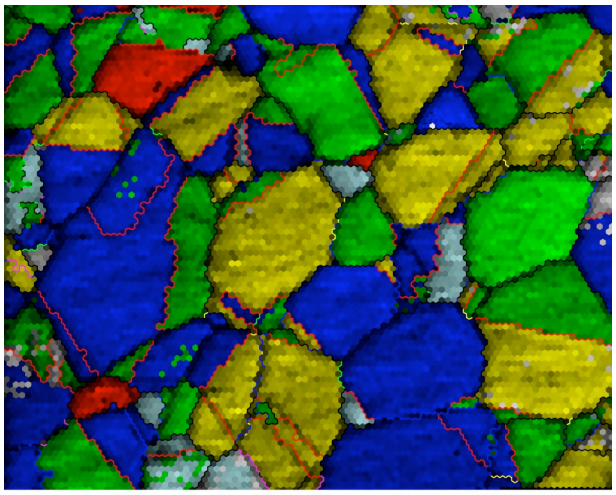

200.0 µm = 25 steps Boundary levels: 15°
IQ 17.2...60, Direction

(b)

Gray Scale Map Type: Image Quality
17.2...60 (17.2...60)

Color Coded Map Type: Crystal Direction

Direction	Min	Max	Total Fraction	Partition Fraction
<1 0 0>|||[0 0 1]	0°	15°	0.029	0.029
<0 1 1>|||[0 0 1]	0°	15°	0.288	0.288
<1 1 1>|||[0 0 1]	0°	15°	0.040	0.040
<1 1 2>|||[0 0 1]	0°	15°	0.267	0.267
<1 1 4>|||[0 0 1]	0°	15°	0.352	0.352

Boundaries: Rotation Angle

Min	Max	Fraction
15°	180°	0.982

Boundaries: CSL

Sigma	Tolerance	Fraction	Volume	MDF Value
1	15.00	0.018	0.0228	0.80
3	8.66	0.340	0.0176	19.38
5	6.71	0.019	0.0123	1.57
7	5.67	0.003	0.0099	0.33
11	4.52	0.005	0.0075	0.61
13a	4.16	0.004	0.0029	1.47
13b	4.16	0.003	0.0039	0.84
15	3.87	0.011	0.0094	1.15
17a	3.64	0.000	0.0020	0.00
17b	3.64	0.004	0.0039	0.97
19a	3.44	0.003	0.0033	0.92
19b	3.44	0.002	0.0022	0.69
21a	3.27	0.002	0.0019	0.80
21b	3.27	0.006	0.0057	1.02
23	3.13	0.007	0.0050	1.32
25a	3.00	0.009	0.0011	8.52
25b	3.00	0.002	0.0044	0.40
9	5.00	0.020	0.0102	2.02
27a	2.89	0.007	0.0020	3.36
27b	2.89	0.007	0.0039	1.81
summary	-	0.471	0.1317	3.58

*For statistics - any point pair with misorientation exceeding 10° is considered a boundary

(c)

Figure 26. OIM map from Alloy 600 (a), map showing the grain orientations (b), and legends for grain orientations and grain boundary character distributions (c).